

UC San Diego

UC San Diego Previously Published Works

Title

FluxSat: Measuring the Ocean-Atmosphere Turbulent Exchange of Heat and Moisture from Space

Permalink

<https://escholarship.org/uc/item/1vr2n2p8>

Journal

Remote Sensing, 12(11)

ISSN

2072-4292

Authors

Gentemann, Chelle L
Clayson, Carol Anne
Brown, Shannon
et al.

Publication Date

2020






DOI

10.3390/rs12111796

Peer reviewed

Article

FluxSat: Measuring the Ocean–Atmosphere Turbulent Exchange of Heat and Moisture from Space

Chelle L. Gentemann ^{1,2,*}, Carol Anne Clayson ³, Shannon Brown ⁴, Tong Lee ⁴ , Rhys Parfitt ⁵, J. Thomas Farrar ³ , Mark Bourassa ⁵ , Peter J. Minnett ⁶ , Hyodae Seo ³ , Sarah T. Gille ⁷ and Victor Zlotnicki ⁴

¹ Farallon Institute, Petaluma, CA 94952, USA

² Earth and Space Research, Seattle WA 98105, USA

³ Department of Physical Oceanography, Woods Hole Oceanographic Institution, Woods Hole, MA 02543, USA; cclayson@whoi.edu (C.A.C.); jfarrar@whoi.edu (J.T.F.); hseo@whoi.edu (H.S.)

⁴ Jet Propulsion Laboratory, California Institute of Technology, Pasadena, CA 91109, USA; Shannon.T.Brown@jpl.nasa.gov (S.B.); tong.lee@jpl.nasa.gov (T.L.); victor.zlotnicki@jpl.nasa.gov (V.Z.)

⁵ Department of Earth, Ocean and Atmospheric Science, Florida State University, Tallahassee, FL 32306, USA; rparfitt@fsu.edu (R.P.); bourassa@coaps.fsu.edu (M.B.)

⁶ Department of Ocean Sciences at the Rosenstiel School of Marine and Atmospheric Science, University of Miami, Miami, FL 33149, USA; pminnett@miami.edu

⁷ Scripps Institution of Oceanography, University of California San Diego, La Jolla, CA 92093-0230, USA; sgille@ucsd.edu

* Correspondence: cgentemann@faralloninstitute.org

Received: 6 May 2020; Accepted: 28 May 2020; Published: 3 June 2020



Abstract: Recent results using wind and sea surface temperature data from satellites and high-resolution coupled models suggest that mesoscale ocean–atmosphere interactions affect the locations and evolution of storms and seasonal precipitation over continental regions such as the western US and Europe. The processes responsible for this coupling are difficult to verify due to the paucity of accurate air–sea turbulent heat and moisture flux data. These fluxes are currently derived by combining satellite measurements that are not coincident and have differing and relatively low spatial resolutions, introducing sampling errors that are largest in regions with high spatial and temporal variability. Observational errors related to sensor design also contribute to increased uncertainty. Leveraging recent advances in sensor technology, we here describe a satellite mission concept, FluxSat, that aims to simultaneously measure all variables necessary for accurate estimation of ocean–atmosphere turbulent heat and moisture fluxes and capture the effect of oceanic mesoscale forcing. Sensor design is expected to reduce observational errors of the latent and sensible heat fluxes by almost 50%. FluxSat will improve the accuracy of the fluxes at spatial scales critical to understanding the coupled ocean–atmosphere boundary layer system, providing measurements needed to improve weather forecasts and climate model simulations.

Keywords: air–sea interactions; mesoscale; fluxes

1. Introduction

The atmosphere and ocean exchange momentum, heat, moisture, and gases. These exchanges play critical roles in the integrated Earth system by affecting the energy, water, and biogeochemical (including carbon) cycles. The momentum exchange (i.e., ocean surface wind stress) is predominantly from the atmosphere to the ocean, resulting in wind-generated ocean currents, upper-ocean mixing, and wind-driven surface waves, but, while this momentum loss acts as a “brake” to the atmosphere, ocean-driven small-scale changes in the wind greatly enhance small-scale coupling between the ocean

and atmosphere. In the tropics, the ocean and atmosphere are tightly coupled, with the atmosphere forcing the ocean primarily through wind stress and the ocean providing feedback to the atmosphere through heat and moisture fluxes, which then impact the marine boundary layer. In the eastern tropical Pacific Ocean, a prominent example is the heat and moisture fluxes associated with El Niño–Southern Oscillation that feed back to the Walker Circulation, influencing weather and precipitation patterns around the world. At mid-latitudes, much of the large-scale ocean variability on decadal and shorter time scales has been considered as a passive response to stochastic atmospheric forcing (e.g., [1–3]). However, satellite observations have revealed significant ocean-forced variability of surface fluxes associated with mesoscale sea surface temperature (SST) variability [4–7]. In atmospheric model simulations, there is a distinct change in the character of air–sea heat and moisture fluxes and in atmospheric frontal variability in these regions when the resolutions of the models or SST forcing increase to about 25 km or better [8–10]. Recent modeling studies suggest that mesoscale SSTs affect the atmospheric boundary layer locally as well as inducing remote responses that influence the path of and activities along mid-latitude storm tracks (e.g., [10–13]), with significant implications for weather and precipitation over continental regions such as the western US and Europe.

Air–sea interaction processes vary both regionally and as a function of spatial scale. The SST–wind relationship provides an indication of such dependencies [4,5]. The correlations between observed SST and wind speed show negative values over much of the global ocean (Figure 1a), which signifies that the atmosphere is forcing the ocean [14–16]. At the largest scales, an increase in wind speed reduces SST by enhancing ocean-to-atmosphere heat fluxes and intensifying the mixing of the warm surface ocean waters with the cooler waters below, and vice versa [17]. However, when both datasets are spatially high-pass-filtered to remove this large-scale SST–wind relationship, the correlations between SST and wind speeds switch sign to reveal positive values over much of the global ocean, especially in regions of significant ocean eddy and frontal activities, such as the eastern equatorial Pacific and Atlantic Oceans, western boundary currents in the mid-latitudes, western Arabian Sea, and much of the Southern Ocean (Figure 1b; [5,18]). These positive correlations reflect the ocean forcing the atmosphere. As winds blow across a mesoscale SST front, an increase in SST increases the vertical mixing of momentum in the atmospheric boundary layer, thereby drawing stronger winds from the higher levels down to the ocean surface and increasing ocean surface wind speed [4,5]. A decrease in SST produces the opposite effect.

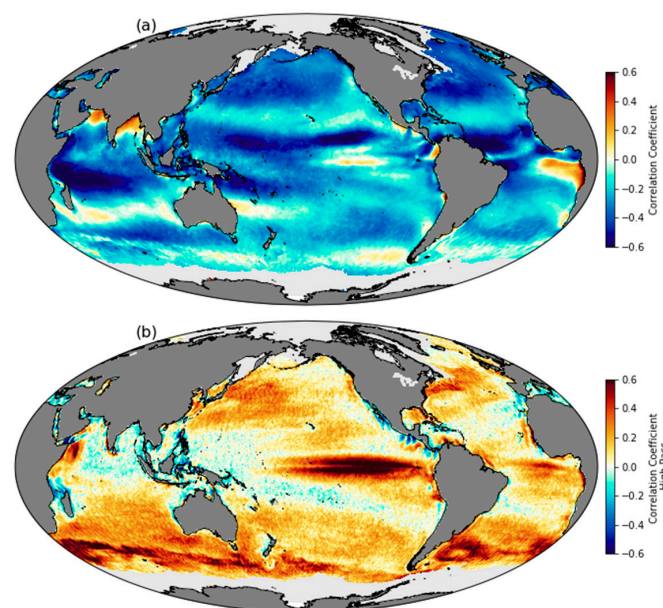


Figure 1. (a) Correlation between QuikScat wind speed [19] and NOAA Optimum Interpolated (OI) SST [20] using daily, 25-km-gridded data from 2000–2009. (b) The same data, using zonally high-pass-filtered

(1000 km cutoff) data. A negative correlation coefficient is expected when the atmosphere forces the ocean (e.g., strong winds drive ocean mixing and cool SST), while a positive correlation coefficient is expected when the ocean forces the atmosphere (e.g., warm SST drives atmospheric mixing and entrainment of faster winds from aloft). (a) shows that, for most of the globe, the atmosphere is forcing the ocean. (b) focuses on mesoscale variability and shows a completely different view, with the ocean forcing the atmosphere almost globally, except in some well-known extreme conditions, e.g., Gulf of Tehuantepec wind jets. In (b), both the Tropical Pacific and western boundary current regions have the strongest link between the ocean and atmosphere.

The vertical transport of heat, momentum, and gases is efficiently accomplished by turbulence in both the atmosphere and ocean. Convective and wind-driven turbulence drives turbulent air–sea heat fluxes that act to reduce the vertical temperature and humidity gradients at and just above the ocean surface; the fluxes drive differing marine boundary layer responses across SST gradients, reinforcing the atmospheric gradients of winds across the surface gradients. The largest air–sea heat fluxes, and the largest uncertainties in these fluxes, occur in regions with strong gradients in SST, such as the western boundary currents, and under extreme wind conditions or large air–sea temperature and humidity gradients in the vicinity of storms or cold-air outbreaks along coasts (e.g., Figure 2). For example, estimates of air–sea heat fluxes from in situ measurements in the Gulf Stream reveal heat fluxes from the ocean to the atmosphere of more than 1400 W m^{-2} during wintertime cold-air outbreaks [21,22]. Changes in heat fluxes in frontal regions can substantially impact poleward heat and moisture transports and affect rainfall patterns [13].

Satellite observations in the past two decades have revolutionized the understanding of air–sea interactions on a variety of scales, highlighting the importance of these interactions for numerical weather prediction and seasonal-to-subseasonal forecasting [4,23,24]. Despite such progress, a major knowledge gap remains in the understanding of small-scale air–sea heat and moisture fluxes associated with mesoscale SST and their impacts on weather and climate. There is mounting evidence that there are intense interactions between the atmosphere and ocean on the scales of ocean eddies, and the need for improved resolution of observational systems is growing as these scales appear to impact weather and climate simulations (e.g., [25,26]). Recent research relates our inability to accurately represent $\sim 25 \text{ km}$ oceanic forcing of atmospheric features from synoptic to seasonal timescales to our lack of skill in predicting extreme events like drought, flooding, and heat waves [27–32]. There is no comprehensive observational inventory of accurate, instantaneous, 25 km heat flux measurements, and, thus, the net contributions on these scales to air–sea exchanges are essentially unquantified by direct observation. Measuring high-resolution air–sea fluxes will open up an entirely new area of research into air–sea exchanges and parameterizations.

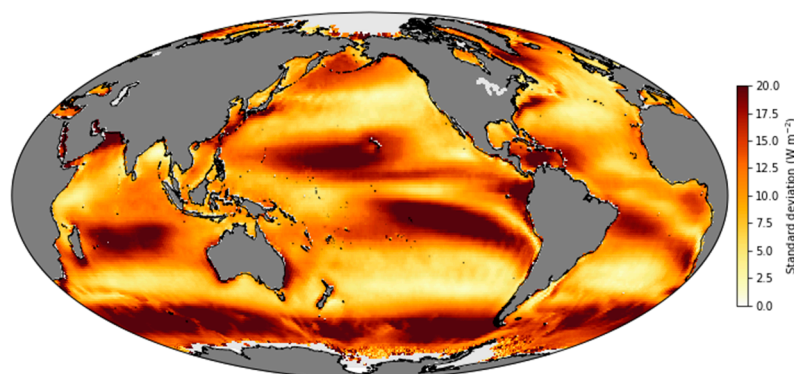


Figure 2. The standard deviation between the climatological mean surface latent heat fluxes between four satellite flux products (HOAPS4 [33,34], SeaFlux Climate Data Record (CDR) [35], IFREMER 4 [36,37], J-OFURO3 [38]), for the 1999–2008 mean. Some of the largest differences between different flux products occur in regions with the largest fluxes.

1.1. Current Status of Flux Estimates

Current satellite-derived flux products are inadequate to evaluate the fidelity of the small-scale flux variability simulated by today's higher-resolution models. Existing satellite-derived flux data products of turbulent air–sea fluxes show large disagreements in high-gradient regions (e.g., [39]; Figure 3). The global satellite-derived air–sea flux datasets are focused on complete global ocean coverage with long-term stable error characteristics, and they use microwave-based retrievals for the atmospheric parameters (with the resolutions as in Table 1). Thus, the SST fields used in the global flux products (as in Figure 3) are typically from lower-resolution microwave fields smoothed and gridded to achieve full global coverage. Moreover, comparisons with buoys near the Gulf Stream and Kuroshio regions show root-mean-square (RMS) differences of $>40 \text{ W m}^{-2}$ in daily averages [39]. Disagreements between the products can occur for multiple reasons. The first reason may be related to differences in techniques for estimating the bulk parameters at the resolution of the individual satellite channel or channels being used for the retrieval. Sea surface temperature is a direct retrieval from satellite radiometer measurements, with different retrieval algorithms and input satellite measurements contributing to differences in the estimated sea surface temperatures [40]. Wind speeds in the global flux products can be derived from either passive or active microwave measurements, or both, but are inferred from wind effects on the surface roughness, with differing retrieval algorithms and satellites contributing to differences between the derived flux fields. Some of the algorithms for deriving global fluxes infer near-surface specific humidity from passive microwave measurements (Hamburg Ocean Atmosphere Parameters and Fluxes from Satellite (HOAPS4; [33,34]) and SeaFlux CDR [35]), while others use reanalysis products or a blend of reanalysis and passive microwave measurements (Institut Français pour la Recherche et l'Exploitation de la Mer, IFREMER 4, [36,37]), and Japanese ocean flux data set using remote-sensing observations (J-OFURO3, [38]). Near-surface air temperature is most commonly estimated using reanalysis products (IFREMER4, J-OFURO3), by using an air–sea temperature difference derived from SST (HOAPS4) or a neural net retrieval from passive microwave (SeaFlux CDR). Errors have typically been ascribed mainly to errors in near-surface air temperature and humidity (e.g., [39]), but errors in wind speed and SST inputs are also important [41].

How the variables are combined can also lead to errors and differences among the products. The input variables for these products have varying spatial resolutions, from at best the roughly-25 km microwave satellite retrievals, through the reanalyses products (at 0.75° or coarser resolution), to the smoothing scale used in some of the input SST products, such as the NOAA's Optimum Interpolated SST (OISST) [20,43]. Furthermore, these inputs come from different satellites with different overpass times, adding a temporal mismatch. Satellite flux products approach this issue in a variety of ways, including binning together all observations within a three-hour window (e.g., IFREMER4), taking the data which are closest in time to a 6-hour time step (e.g., HOAPS4), or binning over an entire day (J-OFURO3). Finally, fluxes are calculated using these inputs to the bulk aerodynamic flux algorithm (see Section 2.4), and the resulting fluxes are thus derived from a complicated mixture of variables with different characteristic time and space scales. The result is the “smearing” of input data and, consequently, of the derived fluxes. An example of this effect is shown in Figure 3, which compares the latent and sensible heat fluxes calculated along a ship track across the Gulf Stream with the coincident satellite measurements (from SeaFlux V3, an hourly, 25 km product). The satellite-derived flux estimates, when averaged along this track, are roughly correct, but the details of the sharp increase in fluxes associated with the change in SST (roughly 50 W m^{-2} per $^\circ\text{C}$) are missing. Given our current inability to resolve these features in global flux products, understanding feedback between the ocean and atmosphere at these spatial scales is challenging.

To illustrate the effect of spatial resolution and temporal offset of input variables in flux estimates, a Weather Research and Forecasting (WRF) model simulation [44] was made over the Gulf Stream extension region, forced by JPL's Multi-scale Ultra-high-Resolution (MUR) SST [45] for the period from 26 November to 10 December 2017. The model domain, shown in Figure 4, has a 3-km resolution with lateral boundary conditions taken from the ERA-Interim atmospheric reanalysis [43]. We first

calculated the latent and sensible heat fluxes from the simultaneous outputs of SST, wind speed, surface air temperature and relative humidity averaged onto a 0.125-degree resolution at 30-min intervals. The time-mean gradients of latent and sensible heat fluxes are shown in Figure 4a,b. We then re-calculated these fluxes using winds that were sampled with a 3-h offset from the other variables. The root-mean-square differences (RMSD) in latent and sensible heat fluxes between the calculations with and without offset timing of the wind speed are shown in Figure 4c,d. Substantial differences are seen both for latent and sensible heat flux gradients due to the time difference of wind speed. The differences in gradients can exceed $150 \text{ W m}^{-2}/100 \text{ km}$ for latent heat flux and $50 \text{ W m}^{-2}/100 \text{ km}$ for sensible heat flux. The RMSD in flux gradients reflects the impact of the time offset of wind speed on the variability of the flux gradients because the impact of such time offset on the time-mean flux gradients is very small.

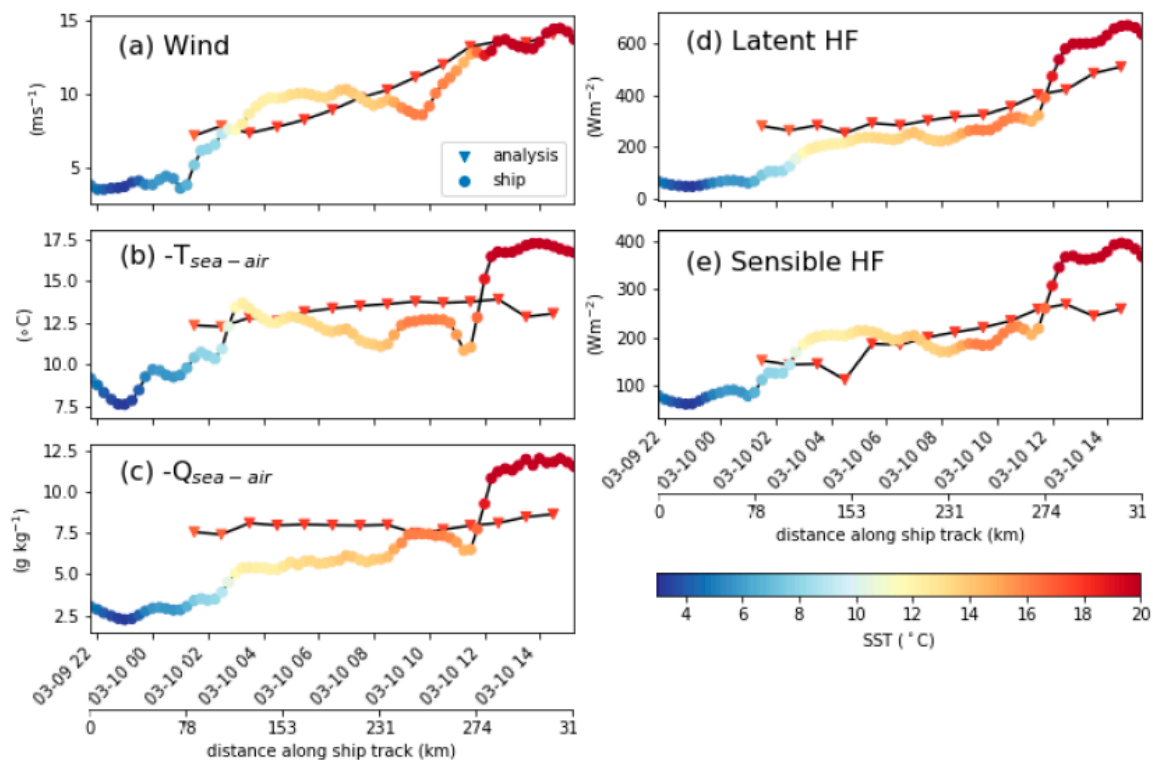


Figure 3. Comparisons between ship-measured (circles) and satellite-derived SeaFlux V3 dataset [42] (triangle) across the Gulf Stream during the CLIMODE experiment [17] for (a) wind speed, (b) sea-air temperature difference, (c) sea-air specific humidity difference, (d) latent heat flux, and (e) sensible heat flux. The satellite-derived variables lack variability compared to the ship-measured variables, which results in reduced gradients in the calculated heat fluxes. The colors of the symbols correspond to the sea surface temperature of the input data stream (either ship or satellite).

Several recent studies have indicated that spatial gradients in heat fluxes are of primary importance in determining the influence of western boundary currents such as the Gulf Stream, not just on the local atmospheric frontal variability, but also on the basin-wide circulation and time-mean atmosphere [10,46]. The effect of spatial resolution on these heat flux gradients can be seen in Figure 4e,f, which shows the time-mean spatial gradients for latent and sensible heat fluxes estimated from the WRF output decimated to 0.5° resolution (current measurement capability corresponds to about 0.5° resolution). Near the Gulf Stream extension, the magnitude of the heat flux gradients estimated from input variables with 0.125° resolution (i.e., Figure 4a,b) are more than a factor of two larger than those estimated from input variables with 0.5° resolution.

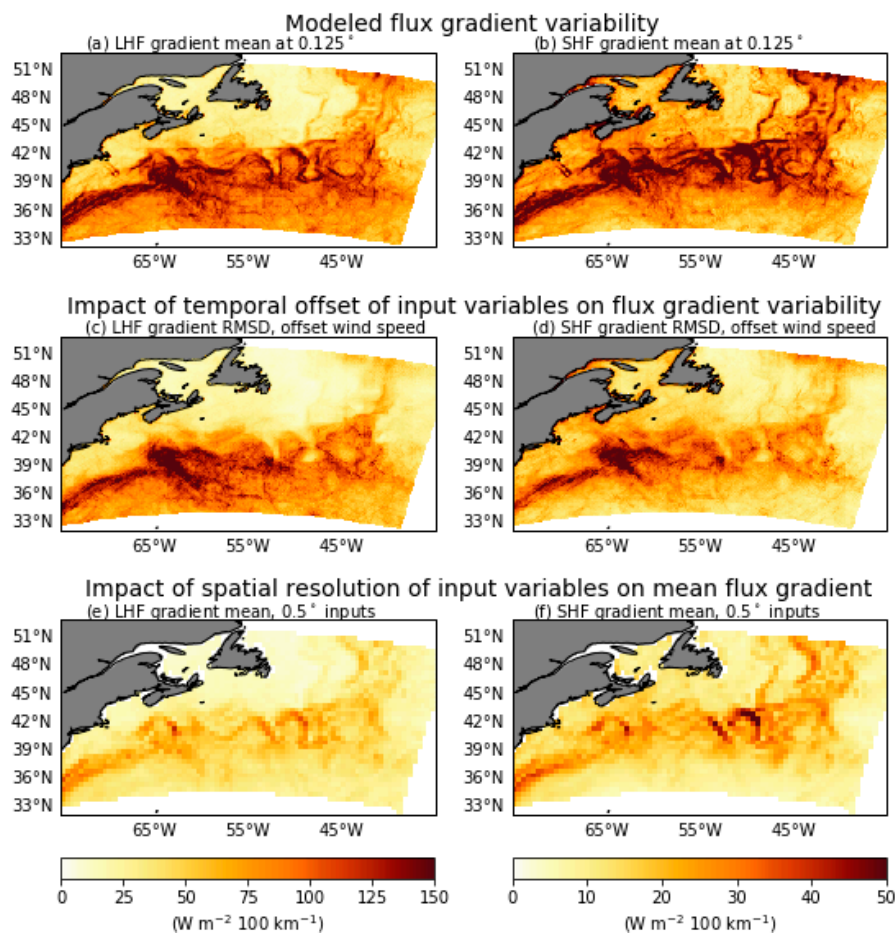


Figure 4. Effect of temporal offsets and spatial resolution on gradients of turbulent heat fluxes. Magnitude of the time-mean (a) latent and (b) sensible heat flux gradients calculated from simultaneous output of wind speed, SST, air temperature and relative humidity at 0.125° resolution. The RMSD in (c) latent and (d) sensible heat flux gradients, with and without offsetting the timing of wind speed from other variables by 3 hours at 0.125° resolution. Magnitude of the time-mean (e) latent and (f) sensible heat flux gradients calculated from simultaneous output of wind speed, SST, air temperature and relative humidity at 0.5° resolution. Note the different ranges in the color bars for latent and sensible heat flux gradients.

The results illustrated by Figure 4 suggest that both time offsets and resolution differences of the input variables can affect the estimated flux gradients, with magnitudes comparable to or larger than $50 \text{ W m}^{-2}/100 \text{ km}$ over widespread areas. For reference, increases in the sensible heat flux gradients on this order in the Gulf Stream region have been found to cause ~30% increases in regional atmospheric frontal frequency and time-mean precipitation in both model and observational studies [9,10].

1.2. Developments Necessary for Significant Progress

Recent community papers call for improving heat and moisture flux estimates [47–49]. Every panel except one in the 2017 Earth Science and Applications from the Space Decadal Survey (hereafter, ESAS Decadal Survey) called for improved measurements of evaporation, boundary layer structure, and/or surface fluxes and the heat and water cycles as components of at least one of their science/societal questions [50]. The ESAS Decadal Survey described 11 “Most Important” or “Very Important” objectives needing improved planetary boundary layer profiles and/or air–sea fluxes (see ESAS Decadal Survey 2017 Table B.1 Consolidated Science and Applications Traceability Matrix, Table 7.2 Priority Targeted Observables Mapped to the Science and Applications Objectives That Were Ranked as Most Important

(MI) or Very Important (VI), and Table 9.1 Summary of Science and Applications Questions and Their Priorities). Different decadal survey objectives required different accuracies and resolutions; priority C-4a calls for the improvement of global air–sea fluxes and sets an aspirational goal of a global accuracy of 5 W m^{-2} for latent and sensible heat fluxes in the mean over a “regional” area, which we interpret as being of the order of an ocean basin. The related measurement objectives for the input variables of near-surface, specific humidity, temperature, and wind were given as 0.3 g kg^{-1} , $0.2 \text{ }^\circ\text{C}$, and 0.1 m s^{-1} accuracies, respectively, for 20 km monthly averages. Achieving this level of resolution and accuracy will require increases in both the resolution and accuracy of satellite observations, as well as improvements in models at these scales.

To meet the ESAS Decadal Survey requirements and overcome present limitations, a purpose-built instrument optimized for measuring parameters that control the surface flux should address the major sources of both observational and sampling errors (Figure 5). Such an instrument would provide data for enhancing the understanding of processes associated with ocean–atmosphere coupling, improving the fidelity of models and as well as weather and climate forecasts, and reducing the uncertainties of flux products. An instrument solution is to combine a traditional low-frequency passive microwave imaging radiometer with a high-spectral resolution imaging microwave sounder for deriving the near-surface ocean and atmosphere properties needed to accurately monitor the turbulent exchange of heat and moisture. Using satellite measurements to simultaneously retrieve the parameters necessary to calculate the sensible and latent heat fluxes (to a precision of $\pm 13 \text{ W m}^{-2}$ and 9 W m^{-2} , respectively), at $<25\text{-km}$ spatial resolution, will provide an entirely new view of how the ocean and atmosphere drive each other, offering unique new measurements of some observables and markedly improved spatial resolution for others (Table 1).

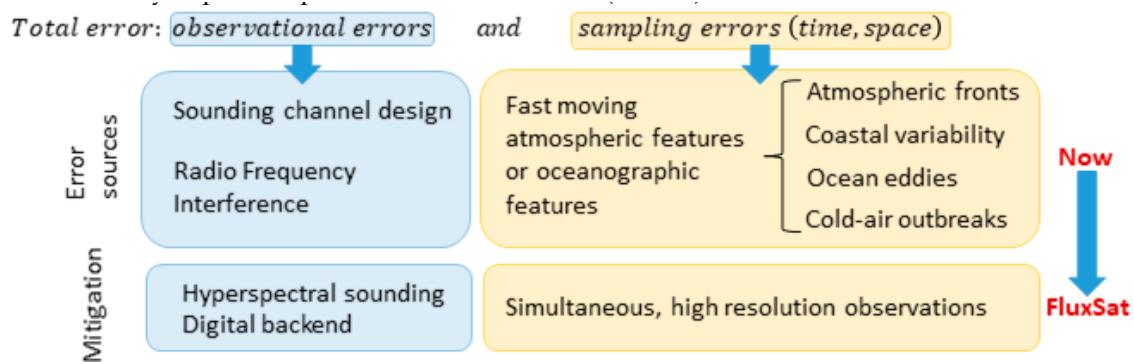


Figure 5. Depiction of turbulent heat and moisture flux error sources and potential future mitigation solutions (e.g., digital backend [51]).

Table 1. Passive microwave radiometer and sounder footprint sizes for flux variables, sea surface temperature, wind speed, near-surface air temperature and near-surface humidity. No single instrument provides all the necessary variables. While all remote sensing measurements have to be translated into geophysical variables, SSMI’s estimates of near-surface air temperature and humidity, as stated in the text above, depend on variables that are also used in calculating fluxes (i.e., wind speed and SST).

Flux Variable	Size (km × km)			
	Aqua AMSRE ¹	WindSAT	SSMI ²	NOAA ATMS ³
T _{sea}	74 × 43	71 × 39	—	—
u	27 × 16	27 × 16	69 × 43	—
T _{air}	—	—	50 × 40	32 (nadir)
q _{air}	—	—	50 × 40	16 (nadir)

¹ Advanced Microwave Scanning Radiometer–Earth Observing System. ² Special Sensor Microwave Imager. ³ Advanced Technology Microwave Sounder.

2. Measuring Turbulent Heat and Moisture Surface Fluxes from Space

2.1. FluxSat

To improve heat and moisture flux observation from space, observational and sampling errors (in time and space) must be reduced. This goal has driven the development of the FluxSat concept. Simultaneous measurements of SST, wind speed, near-surface air temperature and specific humidity could be achieved by a single small satellite (100–500 kg class) with a specially designed passive microwave imager and spectrum-resolving microwave sounder. A conical imaging sensor design using a rotating offset parabolic antenna is preferred to maintain constant spatial resolution over the scan. Calibration requirements for the sensor are expected to be in the same family as those of legacy sensors, enabling use of existing instrument design approaches. Several recent innovations in microwave radiometer/spectrometer technology, combined with advances and small spacecraft systems and launch opportunities, make this concept technologically feasible and affordable as a small focused science investigation. Examples include the Compact Ocean Wind Vector Radiometer (COWVR), which has demonstrated a design for a low-cost conical microwave imager [52]; the Temporal Experiment for Storms and Tropical Systems Demonstration (TEMPEST-D) [53]; and the Time-Resolved Observations of Precipitation structure and storm Intensity with a Constellation of Smallsats (TROPICS) [54], which have demonstrated compact microwave sounders in CubeSats; and CubeSat Radiometer Radio Frequency Interference Technology (CubeRRT), which has demonstrated digital spectrometer technology for observing in the presence of Radio Frequency Interference (RFI), a key issue from 6–37 GHz. One of the things that makes the FluxSat mission concept attractive is that the instrument could be accommodated on a smaller and relatively inexpensive satellite.

2.2. SST and Wind Speed from Passive Microwave Radiometers

Fully-polarimetric 6–37 GHz satellite observations enable the retrieval of ocean vector winds, SST, precipitable water vapor, cloud liquid water, precipitation rate, soil moisture, and sea-ice concentration. The retrieval of these parameters to known accuracies (0.5 K for SST and 0.4 to 0.8 m s⁻¹ for wind speed) has a long heritage and is well established [55–59]. Advances in instrument capabilities (reduced noise and enhanced RFI detection) and new algorithm formulations using machine learning and adaptive algorithm approaches will likely lead to further improvements [58–64]. A significant advance over the capabilities of previous and planned passive microwave radiometers, including the Advanced Microwave Scanning Radiometer-2 (AMSR2), is that the proposed FluxSat 6-GHz and 10-GHz channels include a digital back-end (which digitizes the analog signal), which has the benefit of robustness to Radio Frequency Interference (RFI) as well as having more usable bandwidth to lower noise levels and increased retrieval performance [51].

2.3. Near-Surface Air Temperature and Humidity from a “Hyperspectral” Sounder

Near-surface air temperature and specific humidity are currently estimated using satellite sensors that are not optimized for these parameters. The accuracy of near-surface specific humidity has been estimated at between 0.7 and 1.8 g·kg⁻¹ [33]. Near-surface air temperature accuracy is estimated by comparison to in-situ observations to be 1.3 to 1.55 K [65,66]. FluxSat’s design includes high-spectral resolution microwave sounding spectrometers (often termed “hyperspectral sounders”) at 50 or 118 and 183 GHz that are able to resolve and accurately measure the near-surface air temperature and specific humidity. Many studies have performed information content analysis to demonstrate the value from improved spectral resolution along the wings of oxygen and water vapor absorption lines. A sensor with 162 channels near the 60-GHz line and 114 channels near the 183-GHz band resulted in a 30% variance reduction in boundary layer temperature profile error and a 45% variance reduction in water vapor profile error compared to traditional channelized sensors planned for ESA MetOp [67]. These additional channels were shown to have more than double the information content compared to the 24-channel ESA Microwave Weather Sounder (MWS) [67]. Changing from a 10-channel system

to an 88-channel system results in a 50% reduction in boundary layer temperature and water vapor retrieval error, approaching errors of 0.6 K and 0.58 g kg⁻¹, respectively [68]. A high-spectral resolution sounder can reduce numerical weather prediction, a-priori temperature, and humidity errors by 10–30% [69]. Based on the planned configuration and internal simulations, we expect to achieve accuracies of 0.7 K for near-surface air temperature and 0.58 g kg⁻¹ for near-surface specific humidity.

2.4. Calculating Fluxes

Latent and sensible heat flux would be calculated using a Coupled Ocean–Atmosphere Response Experiment (COARE) 3.5 bulk flux algorithm and the retrieved SST (T_{sea}), equivalent neutral wind speed (u), near-surface air temperature (T_{air}) and near-surface specific humidity (q_{air}), and surface pressure from weather forecast models [70,71] (Figure 6). The impacts of observational errors (Table 2) on fluxes were determined using the formula above a full propagation of errors [33]. The impact of modeled pressure errors is small relative to those of sampling and observational errors (e.g., [72]). Estimates of current random observational errors are taken from the cited literature. The instantaneous latent flux uncertainty for typical ocean conditions is reduced from 24.91 to 13.24 W m⁻², and the sensible flux uncertainty is reduced from 15.55 to 8.63 W m⁻². The improved accuracy of the FluxSat measured variables reduces the observational uncertainty of the fluxes by ~46%. Note that these expected uncertainties are for instantaneous measurements. Spatiotemporal averaging will further reduce the uncertainties. As such, FluxSat represents an important step toward meeting the aspiration goal of the ESAS Decadal Survey 2017 (under C-4a), 5 W m⁻² global accuracy in the mean on local or regional scales for latent and sensible heat fluxes.

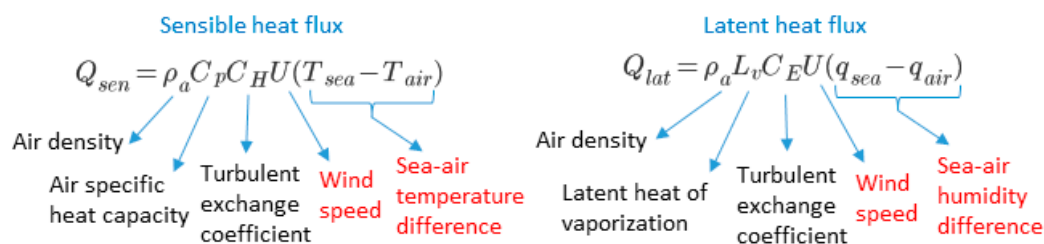


Figure 6. Depiction of turbulent heat and moisture flux equations. The variables in red text need to be measured.

Table 2. Instantaneous observational random uncertainty for each variable and the turbulent fluxes for current missions and the proposed FluxSat mission. The observational random errors for current variables were based on literature cited in the footnotes. Flux uncertainties were calculated using a linear error propagation model provided in the Supplemental Materials, using global average conditions for winds and humidity/temperature differences. It should be noted that the flux uncertainty assumes the only input errors in the current fluxes are due to observational random error, with no estimate of issues associated with temporal/spatial mismatch.

Variable	Observational Random Error		Latent Flux Uncertainty (W m ⁻²)		Sensible Flux Uncertainty (W m ⁻²)	
	Current	FluxSat	Current	FluxSat	Current	FluxSat
q_{sea} (g kg ⁻¹)	0.47 ¹	0.4	6.8	6.1	-	-
q_{air} (g kg ⁻¹)	1.3 ²	0.6	23.2	10.8	-	-
T_{sea} (K)	0.5 ³	0.6	-	-	5.1	4.6
T_{air} (K)	1.6 ⁴	0.7	-	-	14.6	7.2
u (m s ⁻¹)	0.8 ⁵	0.6	5.9	4.4	1.5	1.1
pressure (mb)	5.0	5.0	0.5	0.5	0.1	0.1
total ⁶	-	-	24.9	13.2	15.5	8.6

¹ Calculated using COARE 3 using uncertainties from pressure and T_{sea} . ² Average error from range given in [33]. ³ [57,58]. ⁴ Average error from range given in [64,65]. ⁵ Average error from range given in [55,56]. ⁶ Calculated as the square root of the sum of each error source squared.

3. Implications for New Science

In this section, we discuss three areas of research that could be advanced with high-resolution, accurate heat and moisture surface fluxes from space.

3.1. How Do Unresolved Spatial Gradients in Latent and Sensible Heat Fluxes Affect Weather?

In the high-SST-gradient WBC regions, where much of the small-scale ocean-to-atmosphere forcing can be seen (Figure 1b) turbulent heat and moisture fluxes are climatologically at their largest and most variable [73]. These highly variable fluxes are driven primarily by atmospheric systems on the synoptic time scale [74]. More specifically, extremely large turbulent heat fluxes tend to occur in the lee of atmospheric cold fronts, with strong temperature gradients that rapidly bring cold dry air over warm surface waters [75]. The interaction between the WBCs and these atmospheric fronts is highly coupled, however, with the strong SST gradients associated with the WBCs also exhibiting significant control over the atmospheric fronts through strong gradients in these turbulent heat fluxes (e.g., [10–12]). This is important for many reasons. For example, atmospheric fronts cause up to 90% of the precipitation in mid-latitudes [76]. They also set the time-mean wind convergence and vertical motion throughout the troposphere [46,77], critical for hemispheric circulation [78]. In other words, through atmospheric fronts, WBCs can potentially modulate the atmosphere on all timescales.

Both modelling and reanalysis studies have shown that this frontal air–sea interaction cannot be properly captured at oceanic and atmospheric resolutions that are coarser than ~25 km [8,9]. At scales coarser than this, the associated heat flux gradients cannot be resolved and the atmospheric and oceanic fronts simply cannot “see” each other. Indeed, this makes sense, given that both the cross-frontal scale and ocean mesoscale are ~50–100 km. An obvious example of the importance of resolving frontal-scale gradients can be understood by noting that the suite of models used to inform the IPCC AR5 mostly had oceanic resolution coarser than 100 km. In recent years, there has been an increase in resolution in both models (e.g., HighresMIP [79]) and reanalyses (e.g., ERA-5 [80]). Despite this, however, there is still no way to comprehensively validate improvements in accuracy, as accurate observations of fluxes and their spatial gradients do not exist at the necessary resolution. Until we are able to do so, fluxes and their derivatives in both models and reanalyses remain as uncertain as before, along with the representation of the aforementioned frontal air–sea interaction and its influence on mid-latitude weather and climate.

3.2. How Well Do Existing Operational Numerical Weather Prediction Models Estimate Gradients in Turbulent Heat and Moisture Fluxes?

Existing products show large disagreements with each other in high-gradient regions (e.g., [39]). Comparisons with buoys near the Gulf Stream and Kuroshio regions reported RMS differences of $>40 \text{ W m}^{-2}$ in the daily average. This is also a result of inadequate and incommensurate resolution of the variables that are required to estimate the surface fluxes (e.g., Figures 2 and 3), as well as modeling errors related to two-way air–sea coupling [81]. Furthermore, errors resulting from mismatching, or from ignoring, sub-daily variations in synoptic events or diurnal ocean and atmospheric variability can lead to errors in the mean fluxes [82], affect modeling of variability from diurnal clouds to storms to the Madden–Julian Oscillation (MJO) to El Niño Southern Oscillation (ENSO) [83–85] and extreme events such as drought, flooding, and heat waves [27–31]. Many operational forecast centers are moving to fully coupled models, and determining the accuracy of existing operational numerical weather prediction models should improve our understanding of whether increasing the spatial resolution of fully coupled models will improve the accuracy of weather forecasts from days to seasonal events. Model results indicate that increasing the spatial resolution will improve forecasting of seasonal to subseasonal events, but there currently are no observations to test these results [79].

3.3. How Well Do Existing Flux Products Estimate Turbulent Heat and Moisture Fluxes in High-Gradient Regions?

Satellites have provided data that can be used for estimating global ocean heat and moisture fluxes for more than three decades, and the resulting flux datasets have been used for studies ranging from storm evolution and variability, via upper ocean heat content changes, to estimates used in calculating the state of the global water and energy cycle [86–88]. The flux fields are crucial for understanding the variability of the earth system, from weather and climate variability. However, despite decades of work, large differences still remain between the various fluxes. This is particularly true in regions with high temporal and spatial variability, such as the western boundary current regions (Figure 2). Spatial variability at these important small scales are not captured by existing buoy data, and only a handful of research cruises of short duration have probed variability across high-gradient regions such as the Gulf Stream; even with recent advances in drifting and unmanned vehicles, large numbers of observations that quantify gradient-induced variability in these regions are unlikely in the next decade. A new satellite microwave instrument would provide novel and key measurements allowing a careful quantification of the errors, including the ability to analyze the extent to which temporal/spatial mismatch is a contributor to the differences in the fluxes, in addition to retrieval errors.

At a minimum, FluxSat will allow for better uncertainty quantification of the existing global datasets, which is useful for data assimilation purposes, analyzing the quality of coupled weather and climate models, and improving understanding of climate trends. These data can also be used as a basis for improved retrieval algorithms by providing many more surface measurements than are typically available for analysis using machine learning techniques, which in turn can provide improvements to the global flux products [49]. Lastly, an increased quality of error analysis can provide the basis for improvements to long-term global flux products, providing a significant benefit outside of the few years of this mission.

4. Applications

Growing appreciation of the ocean's impact on our weather and climate has highlighted the importance of understanding air–sea interactions. The data from FluxSat would open up research into air–sea interactions at spatial scales never before measured simultaneously, with high accuracy. While we have discussed some key new areas of science in Sections 2 and 3, these observations could be used in myriad studies related to the turbulent heat exchange, including ocean–wind–driven circulation, thermohaline circulation, high-latitude oceanography, and air–sea–ice exchanges.

There are other research and applied-science applications of the measurements. For example, columnar water vapor, sea ice concentration, precipitation, and soil moisture could be retrieved from FluxSat measurements. These retrievals would enhance the spatiotemporal resolutions of precipitation and soil moisture products and their utility for operational applications, such as flood forecasting, agriculture and irrigation planning, monitoring and forecasting the provision of potable water, solute transport estimation, and Earth system science studies, including coupled land energy and water balance climate studies and hydrology. Such measurements would also enhance the opportunities for interdisciplinary applications, in synergy with other NASA and ESA missions. The combination of flux measurements with those from the Plankton, Aerosol, Cloud and ocean Ecosystem (PACE, [89]) mission would enable research into how phytoplankton communities and carbon uptake are affected by air–sea processes. The flux retrievals and Surface Water and Ocean Topography (SWOT; [90]) observations could be used to investigate how surface air–sea processes on oceanic mesoscales are transmitted into the deeper ocean.

The operational applications of new measurements would include evaluating air–sea sensible and latent heat fluxes and their spatial gradient (especially those associated with oceanic mesoscales) simulated by Numerical Weather Prediction (NWP) models and assessing the impacts of assimilating these measurements on weather forecasting using NWP models and on ocean forecasts using coupled ocean–atmosphere models. Comparing heat fluxes and gradients derived from these new measurements

with the counterparts from the nowcasts and forecasts of NWP models allows for an assessment of the differences between observed and modeled flux spatial gradient magnitudes. The impact these different gradients may have on NWP could be tested using Observing System Sensitivity Experiments (OSSE) that assimilate synthetic measurements and test the impact of such synthetic measurements on weather and ocean forecasting. The synthetic measurements can be obtained from a high-resolution coupled NWP model by sampling it using expected instrument sampling characteristics. Performing Observing System Experiments (OSE) with actual measurements could also test the impacts on weather and ocean forecasts.

5. Conclusions

Currently, most operational NWP model forecasts have limited skill beyond approximately 10 days, partially because today's models do not include the full interaction between ocean and atmosphere. All the major operational weather and climate modeling centers are moving toward fully coupled models with increased spatial and temporal resolution and updating the Earth system models through coupled data assimilation schemes. There is increasing evidence that ocean-forced variability in surface fluxes at approximately 25 km provides important feedback to larger-scale weather systems and could improve forecast skill beyond 10 days. In particular, such feedback could influence precipitation far downstream in the atmospheric circulation.

Right now, we have no way of knowing if these hypothesized interactions are being correctly modelled because observations simply do not exist at the resolution and accuracy needed. FluxSat would provide new, coincident and contemporaneous measurements of all the variables needed to calculate the turbulent sensible and latent heat fluxes at the air–sea interface: wind velocity, SST, near-surface air temperature, and near-surface humidity. This mission is designed to reduce both the observational and sampling errors in the current estimates of latent and sensible heat fluxes. Observational errors will be reduced by providing increased accuracy of the observations and reduction of errors due to RFI. It is important to note that the possible encroachment on protected meteorological bands by the 5-G cellular network would be mitigated by the digital backend to the radiometer. Table 2 shows an ~46% reduction in both latent and sensible observational errors. Sampling errors will be reduced by measuring all the necessary variables from a single platform to provide coincident and contemporaneous measurements. The accurate and highly-resolved air–sea fluxes derived from FluxSat measurements could advance the understanding of the fine-scale nature of the air–sea fluxes, and provide important data for coupled data assimilation to improve forecast skill (e.g., [91,92]).

Important directions for future research were set by the Earth science community in the ESAS Decadal Survey. Surface fluxes were highlighted in all of the decadal survey panels except one and were identified as a topic needing further development. The ESAS Decadal Survey places a heavy emphasis on addressing longer-term changes (e.g., decadal time scales). FluxSat is a first step toward the ESAS Decadal Surveys' aspirational goals: resolving small-scale fluxes and testing the impacts on weather forecast based on a Venture-class mission with a 2-year duration. The science accomplished with this mission would advance our understanding of air–sea interactions and set the stage for other advances that could further address the decadal survey goals. Accurate latent and sensible heat flux observations at <25-km resolution would open up an entirely new area of research into small-scale interactions between the ocean and the atmosphere and provide the critical data needed to understand better the physics of air–sea exchanges.

Supplementary Materials: The scripts and data used to perform the analysis and generate this manuscript are available on https://github.com/cgentemann/2020_FluxSat_MDPI_RemoteSensing and archived in Zenodo. Doi: <http://doi.org/10.5281/zenodo.3840651>; Link: https://github.com/cgentemann/2020_FluxSat_MDPI_RemoteSensing.

Author Contributions: Conceptualization C.L.G. and S.B.; software H.S., C.A.C., C.L.G., and S.B.; writing—original draft preparation, C.L.G.; writing—review and editing C.A.C., S.B., T.L., R.P., J.T.F., M.B., P.J.M., H.S., S.T.G., and V.Z.; Visualization H.S., C.A.C., T.L., and C.L.G. All authors have read and agreed to the published version of the manuscript.

Funding: C.L.G. was funded by NASA grant 80NSSC18K0837. C.A.C. was funded by NASA grants 80NSSC18K0778 and 80NSSC20K0662. J.T.F. was funded by NASA grants NNX17AH54G, NNX16AH76G, and 80NSSC19K1256. S.T.G. was funded by the National Science Foundation grant PLR-1425989 and by the NASA Ocean Vector Winds Science Team grant 80NSSC19K0059. M.B. was funded in part by the Ocean Observing and Monitoring Division, Climate Program Office (FundRef number 100007298), National Oceanic and Atmospheric Administration, U.S. Department of Commerce, and by the NASA Ocean Vector Winds Science Team grant through NASA/JPL. H.S. was funded by National Oceanic and Atmospheric Administration (NOAA) grant NA19OAR4310376 and the Andrew W. Mellon Foundation Endowed Fund for Innovative Research at Woods Hole Oceanographic Institution.

Acknowledgments: Sarah Ann Thompson proofed the paper and formatted references. Caitlin Kroeger helped with the layout of Figures 5 and 6. Part of this research was carried out at the Jet Propulsion Laboratory, California Institute of Technology, under a contract with the National Aeronautics and Space Administration. The authors would like to thank Longtao Wu and Xiaosu Xie of Jet Propulsion Laboratory for conducting the WRF model experiments and data processing, respectively. The MUR SST are available at <https://podaac.jpl.nasa.gov/Multi-scale-Ultra-high-Resolution-MUR-SST>. The QuikScat data 3-day average version 3.0 were downloaded from http://apdrc.soest.hawaii.edu/datadoc/qscat_3day.php. The NOAA High Resolution SST version 2.0 data are provided by the NOAA/OAR/ESRL PSL, Boulder, Colorado, USA, from their Web site at <https://psl.noaa.gov/>, <https://www.ncei.noaa.gov/data/sea-surface-temperature-optimum-interpolation>. The scripts and data used to perform the analysis and generate this manuscript are available on https://github.com/cgentemann/2020_FluxSat_MDPI_RemoteSensing and archived at Zenodo [93].

Conflicts of Interest: The authors declare no conflict of interest. The funders had no role in the design of the study; in the collection, analyses, or interpretation of data; in the writing of the manuscript, or in the decision to publish the results.

References

1. Frankignoul, C.; Müller, P.; Zorita, E. A Simple Model of the Decadal Response of the Ocean to Stochastic Wind Forcing. *J. Phys. Oceanogr.* **1997**, *27*, 1533–1546. [[CrossRef](#)]
2. Barsugli, J.J.; Battisti, D.S. The Basic Effects of Atmosphere–Ocean Thermal Coupling on Midlatitude Variability. *J. Atmos. Sci.* **1998**, *55*, 477–493. [[CrossRef](#)]
3. Ciasto, L.M.; Thompson, D.W.J. North Atlantic Atmosphere–Ocean Interaction on Intraseasonal Time Scales. *J. Clim.* **2004**, *17*, 1617–1621. [[CrossRef](#)]
4. Chelton, D.B.; Schlax, M.G.; Freilich, M.H.; Milliff, R.F. Satellite measurements reveal persistent small-scale features in ocean winds. *Science* **2004**, *303*, 978–983. [[CrossRef](#)]
5. Small, R.J.; deSzoek, S.P.; Xie, S.P.; O’Neill, L.; Seo, H.; Song, Q.; Cornillon, P.; Spall, M.; Minobe, S. Air–sea interaction over ocean fronts and eddies. *Dyn. Atmos. Oceans* **2008**, *45*, 274–319. [[CrossRef](#)]
6. Xie, S.-P. Satellite observations of cool ocean–atmosphere interaction. *Bull. Am. Meteorol. Soc.* **2004**, *85*, 195–208. [[CrossRef](#)]
7. Chelton, D.B.; Xie, S.-P. Coupled ocean–atmosphere interactions at oceanic mesoscales. *Oceanography* **2010**, *23*, 52–69. [[CrossRef](#)]
8. Smirnov, D.; Newman, M.; Alexander, M.A.; Kwon, Y.-O.; Frankignoul, C. Investigating the Local Atmospheric Response to a Realistic Shift in the Oyashio Sea Surface Temperature Front. *J. Clim.* **2014**, *28*, 1126–1147. [[CrossRef](#)]
9. Parfitt, R.; Czaja, A.; Kwon, Y.-O. The impact of SST resolution change in the ERA-Interim reanalysis on wintertime Gulf Stream frontal air–sea interaction. *Geophys. Res. Lett.* **2017**, *44*, 3246–3254. [[CrossRef](#)]
10. Parfitt, R.; Czaja, A.; Minobe, S.; Kuwano-Yoshida, A. The atmospheric frontal response to SST perturbations in the Gulf Stream region. *Geophys. Res. Lett.* **2016**, *43*, 2299–2306. [[CrossRef](#)]
11. Hirata, H.; Kawamura, R.; Yoshioka, M.K.; Nonaka, M.; Tsuboki, K. Key Role of the Kuroshio Current in the Formation of Frontal Structure of an Extratropical Cyclone Associated with Heavy Precipitation. *J. Geophys. Res. Atmos.* **2019**, *124*, 6143–6156. [[CrossRef](#)]
12. Czaja, A.; Frankignoul, C.; Minobe, S.; Vanni re, B. Simulating the Midlatitude Atmospheric Circulation: What Might We Gain From High-Resolution Modeling of Air–Sea Interactions? *Curr. Clim. Chang. Rep.* **2019**, *5*, 390–406. [[CrossRef](#)]
13. O’Reilly, C.H.; Czaja, A. The response of the Pacific storm track and atmospheric circulation to Kuroshio Extension variability. *Q. J. R. Meteorol. Soc.* **2015**, *141*, 52–66. [[CrossRef](#)]
14. Mantua, N.J.; Hare, S.R.; Zhang, Y.; Wallace, J.M.; Francis, R.C. A Pacific interdecadal climate oscillation with impacts on salmon production. *Bull. Am. Meteorol. Soc.* **1997**, *78*, 1069–1079. [[CrossRef](#)]

15. Okumura, Y.; Xie, S.-P.; Numaguti, A.; Tanimoto, Y. Tropical Atlantic air-sea interaction and its influence on the NAO. *Geophys. Res. Lett.* **2001**, *28*, 1507–1510. [[CrossRef](#)]
16. Xie, S.-P. The Shape of Continents, Air-Sea Interaction, and the Rising Branch of the Hadley Circulation. *Hadley Circ. Present Past Future* **2004**, 121–152. [[CrossRef](#)]
17. Cayan, D.R. Latent and Sensible Heat Flux Anomalies over the Northern Oceans: Driving the Sea Surface Temperature. *J. Phys. Oceanogr.* **1992**, *22*, 859–881. [[CrossRef](#)]
18. Seo, H. Distinct Influence of Air–Sea Interactions Mediated by Mesoscale Sea Surface Temperature and Surface Current in the Arabian Sea. *J. Clim.* **2017**. [[CrossRef](#)]
19. Wentz, F.J.; Smith, D.K. A model function for the ocean-normalized radar cross section at 14 GHz derived from NSCAT observations. *J. Geophys. Res. Ocean.* **1999**, *104*, 11499–11514. [[CrossRef](#)]
20. Reynolds, R.W.; Smith, T.M.; Liu, C.; Chelton, D.B.; Casey, K.S.; Schlax, M.G. Daily High-Resolution-Blended Analyses for Sea Surface Temperature. *J. Clim.* **2007**, *20*, 5473–5496. [[CrossRef](#)]
21. Marshall, J.; Ferrari, R.; Forget, G.; Maze, G.; Andersson, A.; Bates, N.; Dewar, W.; Doney, S.; Fratantoni, D.; Joyce, T.; et al. The Climode Field Campaign: Observing the Cycle of Convection and Restratification over the Gulf Stream. *Bull. Am. Meteorol. Soc.* **2009**, *90*, 1337–1350. [[CrossRef](#)]
22. Weller, R.A.; Bigorre, S.P.; Lord, J.; Ware, J.D.; Edson, J.B. A Surface Mooring for Air–Sea Interaction Research in the Gulf Stream. Part I: Mooring Design and Instrumentation. *J. Atmos. Ocean. Technol.* **2012**, *29*, 1363–1376. [[CrossRef](#)]
23. Song, Q.; Chelton, D.B.; Esbensen, S.K.; Thum, N.; O’Neill, L.W. Coupling between sea surface temperature and low-level winds in mesoscale numerical models. *J. Clim.* **2009**, *22*, 146–164. [[CrossRef](#)]
24. Song, Q.; Chelton, D.B.; Esbensen, S.K.; Brown, A.R. An Investigation of the Stability Dependence of SST-Induced Vertical Mixing over the Ocean in the Operational Met Office Model. *J. Clim.* **2016**, *30*, 91–107. [[CrossRef](#)]
25. Yang, P.; Jing, Z.; Wu, L. An Assessment of Representation of Oceanic Mesoscale Eddy–Atmosphere Interaction in the Current Generation of General Circulation Models and Reanalyses. *Geophys. Res. Lett.* **2018**, *45*, 11856–11865. [[CrossRef](#)]
26. Bharti, V.; Fairall, C.W.; Blomquist, B.W.; Huang, Y.; Protat, A.; Sullivan, P.P.; Siems, S.T.; Manton, M.J. Air-Sea Heat and Momentum Fluxes in the Southern Ocean. *J. Geophys. Res. Atmos.* **2019**, *124*, 12426–12443. [[CrossRef](#)]
27. Sugimoto, S.; Aono, K.; Fukui, S. Local atmospheric response to warm mesoscale ocean eddies in the Kuroshio–Oyashio Confluence region. *Sci. Rep.* **2017**, *7*, 1–6. [[CrossRef](#)]
28. Ma, J.; Xu, H.; Dong, C.; Lin, P.; Liu, Y. Atmospheric responses to oceanic eddies in the Kuroshio Extension region. *J. Geophys. Res. Atmos.* **2015**, *120*, 6313–6330. [[CrossRef](#)]
29. Ma, X.; Chang, P.; Saravanan, R.; Montuoro, R.; Hsieh, J.-S.; Wu, D.; Lin, X.; Wu, L.; Jing, Z. Distant Influence of Kuroshio Eddies on North Pacific Weather Patterns? *Sci. Rep.* **2015**, *5*, 17785. [[CrossRef](#)]
30. Steinweg-Woods, J.M. A Lagrangian Analysis of Midlatitude Air-Sea Interaction Associated with Mesoscale Oceanic Eddies. Ph.D. Thesis, Texas A & M University, 2016. Available online: <http://hdl.handle.net/1969.1/157015> (accessed on 28 May 2020).
31. Frenger, I.; Gruber, N.; Knutti, R.; Münnich, M. Imprint of Southern Ocean eddies on winds, clouds and rainfall. *Nat. Geosci.* **2013**, *6*, 608. [[CrossRef](#)]
32. Siqueira, L.; Kirtman, B.P. Atlantic near-term climate variability and the role of a resolved Gulf Stream. *Geophys. Res. Lett.* **2016**, *43*, 3964–3972. [[CrossRef](#)]
33. Liman, J.; Schröder, M.; Fennig, K.; Andersson, A.; Hollmann, R. Uncertainty characterization of HOAPS 3.3 latent heat-flux-related parameters. *Atmos. Meas. Tech.* **2018**, *11*. [[CrossRef](#)]
34. Andersson, A.; Fennig, K.; Klepp, C.; Bakan, S.; Graßl, H.; Schulz, J. The Hamburg Ocean Atmosphere Parameters and Fluxes from Satellite Data—HOAPS-3. *Earth Syst. Sci. Data* **2010**, *2*, 215–234. [[CrossRef](#)]
35. Clayson, C.A.; Brown, J. NOAA Climate Data Record Ocean Surface Bundle (OSB) Climate Data Record (CDR) of Ocean Heat Fluxes, Version 2. *Clim. Algorithm Theor. Basis Doc. C-ATBD Asheville NC NOAA Natl. Cent. Environ. Inf. Doi* **2016**, *10*, V59K4885.
36. Bentamy, A.; Grodsky, S.A.; Katsaros, K.; Mestas-Nuñez, A.M.; Blanke, B.; Desbiolles, F. Improvement in air–sea flux estimates derived from satellite observations. *Int. J. Remote Sens.* **2013**, *34*, 5243–5261. [[CrossRef](#)]
37. Bentamy, A.; Grodsky, S.A.; Elyouncha, A.; Chapron, B.; Desbiolles, F. Homogenization of scatterometer wind retrievals. *Int. J. Climatol.* **2017**, *37*, 870–889. [[CrossRef](#)]

38. Tomita, H.; Hihara, T.; Kako, S.; Kubota, M.; Kutsuwada, K. An introduction to J-OFURO3, a third-generation Japanese ocean flux data set using remote-sensing observations. *J. Oceanogr.* **2019**, *75*, 171–194. [[CrossRef](#)]
39. Bentamy, A.; Piollé, J.F.; Grouazel, A.; Danielson, R.; Gulev, S.; Paul, F.; Azelmat, H.; Mathieu, P.P.; von Schuckmann, K.; Sathyendranath, S.; et al. Review and assessment of latent and sensible heat flux accuracy over the global oceans. *Remote Sens. Environ.* **2017**, *201*, 196–218. [[CrossRef](#)]
40. Merchant, C.J.; Embury, O.; Bulgin, C.E.; Block, T.; Corlett, G.K.; Fiedler, E.; Good, S.A.; Mittaz, J.; Rayner, N.A.; Berry, D.; et al. Satellite-based time-series of sea-surface temperature since 1981 for climate applications. *Sci. Data* **2019**, *6*, 1–18. [[CrossRef](#)]
41. Robertson, F.; Roberts, J.B.; Bosilovich, M.G.; Bentamy, A.; Clayson, C.A.; Fennig, K.; Schröder, M.; Tomita, H.; Compo, G.P.; Gutenstein, M.; et al. Uncertainties in Ocean Latent Heat Flux Variations Over Recent Decades in Satellite-Based Estimates and Reduced Observation Reanalyses. *J. Clim.* in revision.
42. Clayson, C.A.; Roberts, J.B. 2020: SeaFlux V3: A satellite based climate data record of ocean-atmosphere turbulent heat fluxes. in prepare.
43. Skamarock, W.C.; Klemp, J.B.; Dudhia, J.; Gill, D.O.; Barker, D.M.; Wang, W.; Powers, J.G. *A Description of the Advanced Research WRF Version 3* (No. NCAR/TN-475+STR); University Corporation for Atmospheric Research: Boulder, CO, USA, 2008. [[CrossRef](#)]
44. Chin, T.M.; Vazquez-Cuervo, J.; Armstrong, E. A multi-scale high-resolution analysis of global sea surface temperature. *Remote Sens. Environ.* **2017**, *200*, 154–169. [[CrossRef](#)]
45. Dee, D.P.; Uppala, S.M.; Simmons, A.J.; Berrisford, P.; Poli, P.; Kobayashi, S.; Andrae, U.; Balmaseda, M.A.; Balsamo, G.; Bauer, P.; et al. The ERA-Interim reanalysis: Configuration and performance of the data assimilation system. *Q. J. R. Meteorol. Soc.* **2011**, *137*, 553–597. [[CrossRef](#)]
46. Parfitt, R.; Kwon, Y.-O. The modulation of Gulf Stream influence on the troposphere by the eddy-driven jet. *J. Clim.* **2020**. [[CrossRef](#)]
47. Cronin, M.F.; Gentemann, C.L.; Edson, J.; Ueki, I.; Bourassa, M.; Brown, S.; Clayson, C.A.; Fairall, C.W.; Farrar, J.T.; Gille, S.T.; et al. Air-Sea Fluxes With a Focus on Heat and Momentum. *Front. Mar. Sci.* **2019**, *6*. [[CrossRef](#)]
48. Bishop, S.P.; Small, R.J.; Bryan, F.O.; Tomas, R.A.; Bishop, S.P.; Small, R.J.; Bryan, F.O.; Tomas, R.A. Scale Dependence of Midlatitude Air–Sea Interaction. *J. Clim.* **2017**. [[CrossRef](#)]
49. Hagos, S.; Foltz, G.R.; Zhang, C.; Thompson, E.; Seo, H.; Chen, S.; Capotondi, A.; Reed, K.A.; DeMott, C.; Protat, A. Atmospheric Convection and Air–Sea Interactions over the Tropical Oceans: Scientific Progress, Challenges and Opportunities. *Bull. Am. Meteorol. Soc.* **2019**. [[CrossRef](#)]
50. National Academies of Sciences, Engineering, and Medicine. *Thriving on Our Changing Planet: A Decadal Strategy for Earth Observation from Space*; National Academies Press: Washington, DC, USA, 2019; ISBN 978-0-309-46757-5. Available online: <https://www.nap.edu/catalog/24938/thriving-on-our-changing-planet-a-decadal-strategy-for-earth> (accessed on 28 May 2020).
51. Misra, S.; Kocz, J.; Jarnot, R.; Brown, S.T.; Bendig, R.; Felten, C.; Johnson, J.T. Development of an On-Board Wide-Band Processor for Radio Frequency Interference Detection and Filtering. *IEEE Trans. Geosci. Remote Sens.* **2019**, *57*, 3191–3203. [[CrossRef](#)]
52. Brown, S.; Focardi, P.; Kitiyakara, A.; Maiwald, F.; Milligan, L.; Montes, O.; Padmanabhan, S.; Redick, R.; Russel, D.; Bach, V.; et al. The COWVR Mission: Demonstrating the capability of a new generation of small satellite weather sensors. In Proceedings of the 2017 IEEE Aerospace Conference, Big Sky, MT, USA, 4–11 March 2017; IEEE: Big Sky, MT, USA, 2017; pp. 1–7.
53. Padmanabhan, S.; Gaier, T.C.; Reising, S.C.; Lim, B.H.; Stachnik, R.; Jarnot, R.; Berg, W.; Kummerow, C.D.; Chandrasekar, V. Radiometer payload for the temporal experiment for storms and tropical systems technology demonstration mission. In Proceedings of the 2017 IEEE International Geoscience and Remote Sensing Symposium (IGARSS), Fort Worth, TX, USA, 23–28 July 2017; pp. 1213–1215.
54. Blackwell, W.J.; Braun, S.; Bennartz, R.; Velden, C.; DeMaria, M.; Atlas, R.; Dunion, J.; Marks, F.; Rogers, R.; Annane, B.; et al. An overview of the TROPICS NASA Earth Venture Mission. *Q. J. R. Meteorol. Soc.* **2018**, *144*, 16–26. [[CrossRef](#)]
55. Zhang, L.; Shi, H.; Wang, Z.; Yu, H.; Yin, X.; Liao, Q. Comparison of Wind Speeds from Spaceborne Microwave Radiometers with In Situ Observations and ECMWF Data over the Global Ocean. *Remote Sens.* **2018**, *10*, 425. [[CrossRef](#)]

56. Meissner, T.; Wentz, F.J.; Ricciardulli, L. The emission and scattering of L-band microwave radiation from rough ocean surfaces and wind speed measurements from the Aquarius sensor. *J. Geophys. Res. Oceans* **2014**, *119*, 6499–6522. [[CrossRef](#)]
57. Gentemann, C.L. Three way validation of MODIS and AMSR-E sea surface temperatures. *J. Geophys. Res.* **2014**, *119*, 2583–2598. [[CrossRef](#)]
58. Nielsen-Englyst, P.; Høyer, J.L.; Toudal Pedersen, L.; Gentemann, C.L.; Alerskans, E.; Block, T.; Donlon, C. Optimal Estimation of Sea Surface Temperature from AMSR-E. *Remote Sens.* **2018**, *10*, 229. [[CrossRef](#)]
59. Wilheit, T.T.; Chang, A.T.C. An algorithm for retrieval of ocean surface and atmospheric parameters from the observations of the Scanning Multichannel Microwave Radiometer (SMMR). *Radio Sci.* **1980**, *15*, 525–544. [[CrossRef](#)]
60. Shibata, A. Calibration of AMSR-E SST toward a Monitoring of Global Warming. In Proceedings of the 2005 IEEE International Geoscience and Remote Sensing Symposium, Seoul, Korea, 29 July 2005; Volume 5, pp. 3448–3449.
61. Shibata, A. A wind speed retrieval algorithm by combining 6 and 10 GHz data from advanced microwave scanning radiometer: Wind speed inside hurricanes. *J. Oceanogr.* **2006**, *62*, 351–359. [[CrossRef](#)]
62. Wentz, F.J.; Meissner, T. *AMSR-E Ocean Algorithms; Supplement 1*; Remote Sensing Systems: Santa Rosa, CA, USA, 2007; p. 6.
63. Alerskans, E.; Høyer, J.L.; Gentemann, C.L.; Pedersen, L.T.; Nielsen-Englyst, P.; Donlon, C. Construction of a climate data record of sea surface temperature from passive microwave measurements. *Remote Sens. Environ.* **2020**, *236*, 111485. [[CrossRef](#)]
64. Roberts, J.B.; Clayson, C.A.; Robertson, F.R. Improving Near-Surface Retrievals of Surface Humidity Over the Global Open Oceans From Passive Microwave Observations. *Earth Space Sci.* **2019**, *6*, 1220–1233. [[CrossRef](#)]
65. Jackson, D.L.; Wick, G.A. Near-Surface Air Temperature Retrieval Derived from AMSU-A and Sea Surface Temperature Observations. *J. Atmos. Ocean. Technol.* **2010**, *27*, 1769–1776. [[CrossRef](#)]
66. Mahfouf, J.-F.; Birman, C.; Aires, F.; Prigent, C.; Orlandi, E.; Milz, M. Information content on temperature and water vapour from a hyper-spectral microwave sensor. *Q. J. R. Meteorol. Soc.* **2015**, *141*, 3268–3284. [[CrossRef](#)]
67. Tennant, G.; Hurd, D.; Kangas, V. The NWP contribution from the microwave sounder (MWS) on MetOp-Second Generation. In Proceedings of the 2016 14th Specialist Meeting on Microwave Radiometry and Remote Sensing of the Environment (MicroRad), Espoo, Finland, 11–14 April 2016; pp. 115–120.
68. Blackwell, W.J.; Bickmeier, L.J.; Leslie, R.V.; Pieper, M.L.; Samra, J.E.; Surussavadee, C.; Upham, C.A. Hyperspectral Microwave Atmospheric Sounding. *IEEE Trans. Geosci. Remote Sens.* **2011**, *49*, 128–142. [[CrossRef](#)]
69. Aires, F.; Prigent, C.; Orlandi, E.; Milz, M.; Eriksson, P.; Crewell, S.; Lin, C.-C.; Kangas, V. Microwave hyperspectral measurements for temperature and humidity atmospheric profiling from satellite: The clear-sky case. *J. Geophys. Res. Atmos.* **2015**, *120*, 11334–11351. [[CrossRef](#)]
70. Fairall, C.W.; Bradley, E.F.; Hare, J.E.; Grachev, A.A.; Edson, J.B. Bulk parameterization of air-sea fluxes: Updates and verification for the COARE algorithm. *J. Clim.* **2003**, *16*, 571–591. [[CrossRef](#)]
71. Edson, J.B.; Jampana, V.; Weller, R.A.; Bigorre, S.P.; Plueddemann, A.J.; Fairall, C.W.; Miller, S.D.; Mahrt, L.; Vickers, D.; Hersbach, H. On the Exchange of Momentum over the Open Ocean. *J. Phys. Oceanogr.* **2013**, *43*, 1589–1610. [[CrossRef](#)]
72. Colbo, K.; Weller, R.A. Accuracy of the IMET Sensor Package in the Subtropics. *J. Atmos. Ocean. Technol.* **2009**, *26*, 1867–1890. [[CrossRef](#)]
73. Yu, L.; Weller, R.A. Objectively Analyzed Air–Sea Heat Fluxes for the Global Ice-Free Oceans (1981–2005). *Bull. Am. Meteorol. Soc.* **2007**. [[CrossRef](#)]
74. Shaman, J.; Samelson, R.M.; Skillingstad, E. Air–Sea Fluxes over the Gulf Stream Region: Atmospheric Controls and Trends. *J. Clim.* **2010**, *23*, 2651–2670. [[CrossRef](#)]
75. Parfitt, R.; Czaja, A. On the contribution of synoptic transients to the mean atmospheric state in the Gulf Stream region. *Q. J. R. Meteorol. Soc.* **2016**, *142*, 1554–1561. [[CrossRef](#)]
76. Catto, J.L.; Pfahl, S. The importance of fronts for extreme precipitation. *J. Geophys. Res. Atmos.* **2013**, *118*, 10791–10801. [[CrossRef](#)]

77. Parfitt, R.; Seo, H. A New Framework for Near-Surface Wind Convergence Over the Kuroshio Extension and Gulf Stream in Wintertime: The Role of Atmospheric Fronts. *Geophys. Res. Lett.* **2018**, *45*, 9909–9918. [[CrossRef](#)]
78. Lee, R.W.; Woollings, T.J.; Hoskins, B.J.; Williams, K.D.; O'Reilly, C.H.; Masato, G. Impact of Gulf Stream SST biases on the global atmospheric circulation. *Clim. Dyn.* **2018**, *51*, 3369–3387. [[CrossRef](#)]
79. Haarsma, R.J.; Roberts, M.J.; Vidale, P.L.; Senior, C.A.; Bellucci, A.; Bao, Q.; Chang, P.; Corti, S.; Fučkar, N.S.; Guemas, V.; et al. High Resolution Model Intercomparison Project (HighResMIP v1.0) for CMIP6. *Geosci. Model Dev.* **2016**, *9*, 4185–4208. [[CrossRef](#)]
80. Hersbach, H.; Dee, D. ERA5 reanalysis is in production. *ECMWF Newsletter*; Shinfield Park: Reading, UK, 2016. Available online: <https://www.ecmwf.int/en/newsletter/147/news/era5-reanalysis-production> (accessed on 15 April 2020).
81. Shi, Q.; Bourassa, M.A. Coupling Ocean Currents and Waves with Wind Stress over the Gulf Stream. *Remote Sens.* **2019**, *11*, 1476. [[CrossRef](#)]
82. Clayson, C.A.; Bogdanoff, A.S. The Effect of Diurnal Sea Surface Temperature Warming on Climatological Air–Sea Fluxes. *J. Clim.* **2012**, *26*, 2546–2556. [[CrossRef](#)]
83. Ruppert, J.H.; Johnson, R.H. On the cumulus diurnal cycle over the tropical warm pool. *J. Adv. Model. Earth Syst.* **2016**, *8*, 669–690. [[CrossRef](#)]
84. DeMott, C.A.; Benedict, J.J.; Klingaman, N.P.; Woolnough, S.J.; Randall, D.A. Diagnosing ocean feedbacks to the MJO: SST-modulated surface fluxes and the moist static energy budget. *J. Geophys. Res. Atmos.* **2016**, *121*, 8350–8373. [[CrossRef](#)]
85. Tian, F.; von Storch, J.-S.; Hertwig, E. Impact of SST diurnal cycle on ENSO asymmetry. *Clim. Dyn.* **2019**, *52*, 2399–2411. [[CrossRef](#)]
86. Von Schuckmann, K.; Palmer, M.D.; Trenberth, K.E.; Cazenave, A.; Chambers, D.; Champollion, N.; Hansen, J.; Josey, S.A.; Loeb, N.; Mathieu, P.-P.; et al. An imperative to monitor Earth's energy imbalance. *Nat. Clim. Chang.* **2016**, *6*, 138–144. [[CrossRef](#)]
87. Rodell, M.; Beaudoin, H.K.; L'Ecuyer, T.S.; Olson, W.S.; Famiglietti, J.S.; Houser, P.R.; Adler, R.; Bosilovich, M.G.; Clayson, C.A.; Chambers, D.; et al. The Observed State of the Water Cycle in the Early Twenty-First Century. *J. Clim.* **2015**, *28*, 8289–8318. [[CrossRef](#)]
88. L'Ecuyer, T.S.; Beaudoin, H.K.; Rodell, M.; Olson, W.; Lin, B.; Kato, S.; Clayson, C.A.; Wood, E.; Sheffield, J.; Adler, R.; et al. The Observed State of the Energy Budget in the Early Twenty-First Century. *J. Clim.* **2015**, *28*, 8319–8346. [[CrossRef](#)]
89. Werdell, P.J.; Behrenfeld, M.J.; Bontempi, P.S.; Boss, E.; Cairns, B.; Davis, G.T.; Franz, B.A.; Gliese, U.B.; Gorman, E.T.; Hasekamp, O.; et al. The Plankton, Aerosol, Cloud, Ocean Ecosystem Mission: Status, Science, *Advances. Bull. Am. Meteorol. Soc.* **2019**, *100*, 1775–1794. [[CrossRef](#)]
90. Morrow, R.; Fu, L.-L.; Arduin, F.; Benkiran, M.; Chapron, B.; Cosme, E.; d'Ovidio, F.; Farrar, J.T.; Gille, S.T.; Lapeyre, G.; et al. Global Observations of Fine-Scale Ocean Surface Topography With the Surface Water and Ocean Topography (SWOT) Mission. *Front. Mar. Sci.* **2019**, *6*. [[CrossRef](#)]
91. Smith, P.J.; Fowler, A.M.; Lawless, A.S. Exploring strategies for coupled 4D-Var data assimilation using an idealised atmosphere–ocean model. *Tellus Dyn. Meteorol. Oceanogr.* **2015**, *67*, 27025. [[CrossRef](#)]
92. Penny, S.G.; Bach, E.; Bhargava, K.; Chang, C.-C.; Da, C.; Sun, L.; Yoshida, T. Strongly Coupled Data Assimilation in Multiscale Media: Experiments Using a Quasi-Geostrophic Coupled Model. *J. Adv. Model. Earth Syst.* **2019**, *11*, 1803–1829. [[CrossRef](#)]
93. Gentemann, C.L. cgentemann/2020_FluxSat_MDPI_RemoteSensing: Initial_release (Version v1.0). *Zenodo* **2020**. [[CrossRef](#)]

